A Portable CMOS-Based Spin Resonance System for High-Resolution Spectroscopy and Imaging

Daniel Krüger, *Graduate Student Member, IEEE*, Aoyang Zhang, *Member, IEEE*, Behdad Aghelnejad, Henry Hinton, *Graduate Student Member, IEEE*, Victor Marrugat Arnal, Yi-Qiao Song, Yiqiao Tang, Ka-Meng Lei, *Senior Member, IEEE*, Jens Anders, *Senior Member, IEEE*, and Donhee Ham, *Fellow, IEEE*

***Abstract*— Nuclear magnetic resonance (NMR) is a paramount analytical tool for chemistry, biology, medicine, and geology, and has a fundamental importance in physics. The recent years have seen a wealth of efforts to miniaturize NMR systems by combining permanent magnets and CMOS radio frequency (RF)-integrated circuits (ICs) to make the benefit of NMR more broadly available beyond dedicated facilities, which have resulted in systems capable of NMR relaxometry first, and later NMR spectroscopy, the two key NMR modalities. Here we report a small NMR system comprising a digitally assisted CMOS RF transceiver IC and a 0.51-T permanent magnet, which not only enhances spectroscopy and relaxometry performance but also includes magnetic resonance imaging (MRI), a powerful variant of relaxometry. The system achieves a spectral resolution of <0.05 ppm (1.1 Hz), the highest reported in a portable CMOS-based NMR system, and an imaging resolution of 67 × 67 × 83 μm^3.**

***Index Terms*— Bioelectronics, CMOS-integrated circuit (IC), magnetic resonance imaging (MRI), nuclear magnetic resonance (NMR), radio frequency (RF) IC.**

I. Introduction

With the power to elucidate molecular structures and probe material compositions, nuclear magnetic resonance (NMR) revolutionized organic chemistry, structural biology, medical imaging, and subsurface exploration [1], [2], [3], [4], [5], [6], [7], [8], [9]. NMR is also of importance to physics where it originated [10], [11], [12], [13]; a rich repertoire of quantum state manipulation techniques developed for NMR are used in atomic, molecular, and optical physics, as well as for quantum computing [14].

The proton—the nucleus of a ^{1}H atom—has a magnetic moment $\vec{\mu}$ due to its spin $\vec{S}$ ($\vec{\mu} = \gamma\vec{S}$; γ: proton's gyromagnetic ratio). Thus when a ^{1}H atom is placed in a static magnetic field B_0, $\vec{\mu}$ preferentially lines up along B_0 to minimize energy. Subsequently, if an radio frequency (RF) magnetic field with frequency tuned close to $f_0 = \gamma B_0/(2\pi)$ is applied ($f_0 \approx 42$ MHz for $B_0 = 1$ T) in the direction perpendicular to B_0, $\vec{\mu}$ is tilted away from the B_0 direction, increasing energy. After this resonant excitation, $\vec{\mu}$, now having an angle with B_0, precesses about B_0 at f_0, which can be measured. The RF excitation and follow-on readout of the RF precession are the key elements of any NMR experiment. Thus, an NMR instrument consists of a B_0-producing magnet, a coil around a sample, and an RF transceiver. During excitation, the RF transmitter drives the coil to produce the excitation RF magnetic field. During readout, the $\vec{\mu}$ precession induces a sinusoidal voltage in the coil, which is picked up by the RF receiver.

NMR experiments are categorized into spectroscopy, relaxometry, and magnetic resonance imaging (MRI). Imagine an organic molecule containing ^{1}H atoms. As the molecule produces, effectively, a number of tiny local static magnetic fields according to its structure and adds them to B_0, ^{1}H proton spins in the molecule exhibit a number of precession frequencies slightly different from $f_0 = \gamma B_0/(2\pi)$. By measuring them, one can determine the magnetic fields produced by the molecule, and thus the molecular structure. This **spectroscopy** transformed organic chemistry and structural biology.

The precession signal from a sample containing many ^{1}H proton spins is gradually damped with a characteristic relaxation time called T_2. The damping arises mainly due to the loss of phase coherence among precessing spins. The rate of phase decoherence varies with material species containing ^{1}H protons (e.g., water versus fat). Thus T_2 measurement, or **relaxometry**, is used to interrogate material compositions.

MRI is a variant of relaxometry. T_2 measurements at different positions across a body part produce a spatial heat map of T_2 (e.g., if fat contents vary spatially, so does T_2). This is an MRI image. To measure T_2 at different positions, the static magnetic field is provided with spatial gradients. Then

Manuscript received 6 January 2023; revised 26 March 2023; accepted 25 April 2023. Date of publication 17 May 2023; date of current version 28 June 2023. This article was approved by Associate Editor Makoto Nagata. This work was supported in part by the Advanced Research Projects Agency-Energy (ARPA-E) under Contract DE-AR0001063 and in part by the University of Macau under Grant MYRG2020-00132-IME. The work of Victor Marrugat Arnal was supported by the Centre de Formació Interdisciplinària Superior (CFIS)-Universitat Politécnica de Catalunya (UPC) through the Exchange Program at Harvard University. *(Corresponding author: Donhee Ham.)*

Daniel Krüger is with the Harvard John A. Paulson School of Engineering and Applied Sciences, Harvard University, Cambridge, MA 02138 USA, and also with the Institute of Smart Sensors, University of Stuttgart, 70569 Stuttgart, Germany.

Aoyang Zhang, Henry Hinton, Yi-Qiao Song, and Donhee Ham are with the Harvard John A. Paulson School of Engineering and Applied Sciences, Harvard University, Cambridge, MA 02138 USA (e-mail: donhee@seas.harvard.edu).

Behdad Aghelnejad was with the Harvard John A. Paulson School of Engineering and Applied Sciences, Harvard University, Cambridge, MA 02138 USA. He is now with Oxford Instruments, OX13 5QX Abingdon, U.K.

Victor Marrugat Arnal was with the Harvard John A. Paulson School of Engineering and Applied Sciences, Harvard University, Cambridge, MA 02138 USA. He is now with ETH Zurich, 8092 Zurich, Switzerland.

Yiqiao Tang was with the Schlumberger-Doll Research, Cambridge, MA 02139 USA. He is now with Meta, Menlo Park, CA 94025 USA.

Ka-Meng Lei is with the State Key Laboratory of Analog and Mixed-Signal VLSI, Institute of Microelectronics, and the Department of ECE, Faculty of Science and Technology, University of Macau, Macau, China.

Jens Anders is with the Institute of Smart Sensors, University of Stuttgart, 70569 Stuttgart, Germany.

Color versions of one or more figures in this article are available at https://doi.org/10.1109/JSSC.2023.3274043.

Digital Object Identifier 10.1109/JSSC.2023.3274043

the NMR frequency is a function of position, and specific positions to perform relaxometry can be resonantly selected.

Despite such powerful usage, NMR has been largely limited to dedicated facilities, as its instruments are bulky, heavy, and expensive. For example, a state-of-the-art NMR spectroscopy system relies on a large superconducting magnet to obtain a strong and homogeneous static magnetic field, as the field strength enhances the NMR signal and the field homogeneity is needed to resolve the spectral peaks around f_0. An MRI system also typically utilizes a large superconducting magnet with its bore accommodating a human body, although the field strength requirement is not as stringent as in spectroscopy and the field homogeneity is deliberately broken with the gradient.

To bring the benefit of NMR more broadly, a wealth of efforts have been recently dedicated to miniaturizing NMR systems [15], [16], [17], [18], [19], [20], [21], [22], [23], [24]. The strategy is to replace large superconducting magnets with small permanent magnets with sufficient field homogeneity and discrete RF transceiver electronics with integrated RF transceiver chips. For example, we combined permanent magnets and CMOS RF transceiver-integrated circuits (ICs) to develop a series of portable NMR systems, originally capable of only relaxometry [18], [19], [20], [21], [22], and later capable of both relaxometry and spectroscopy [23].

In the present article—as an expansion of a conference paper [25]—we report a new portable NMR system (see Fig. 1) combining a 0.51-T permanent magnet ($f_0 \approx 21.8$ MHz) and a CMOS RF transceiver IC, whose NMR functions now include relaxometry, spectroscopy, and MRI. For MRI, it achieves a spatial image resolution of $67 \times 67 \times 83$ μm^3. For spectroscopy, it reaches a spectral resolution of 0.05 ppm (1.1 Hz), the highest among portable CMOS-based NMR systems reported so far (the prior record was 0.13 ppm [23]). As a small spectroscopy system relying on the weak field of the permanent magnet, it cannot be used to determine structures of macromolecules (e.g., protein), but it enables on-demand fingerprinting of small molecules. As a small MRI system (occupying less than 5 L and weighing less than 10 kg, it is 2700× smaller and 480× lighter than a preclinical MRI system, and even smaller/lighter than a medical MRI system), it cannot accommodate a human body but can be useful for imaging small organisms, organoids, and biopsied tissues.

Critical to the development of this multimodal NMR platform is not only the overall instrument engineering but also the design of the CMOS RF transceiver IC that runs the instrument. The RF receiver should be highly sensitive to detect a precession signal that is weak due to the small B_0 of the permanent magnet, yet must feature a large dynamic range to handle different sample volumes for different NMR modalities. The RF transmitter must efficiently modulate its output amplitude and phase to produce complex temporal patterns of the excitation RF magnetic field for versatile manipulation of $\vec{\mu}$ for varying sample volumes and different NMR modalities to determine molecular structures and material compositions. The IC must be also capable of field gradient control for MRI. Equally importantly, the transmitter's temporal excitation patterns and the receiver's precession readouts (and the gradient control in case of MRI) must be orchestrated altogether with

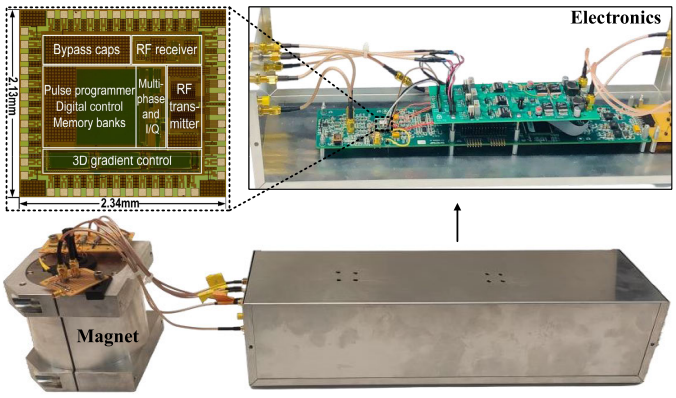

Fig. 1. Overall system.

timing synchronizations. For such orchestration to be efficient, the IC should integrate memory banks to store the orchestration instruction, and digital logic to translate the instruction. Implementation that meets these complex RF, mixed-signal, and digital requirements is at the heart of the CMOS RF transceiver IC developed in the present work. This IC is a significant advance from our previous state-of-the-art IC used in both [23] (for relaxometry and spectroscopy) and [24] (for relaxometry, spectroscopy, and MRI but with OFF-chip field gradient control for MRI). The advance lies not only in the ON-chip field gradient control, but also in the digitally assisted transmitter architecture, digital logic with multiloop features, and improved memory operation. Of note, [26] reports an NMR IC in the same league of complexity as the present work, but its system lacks spectroscopy capability.

Section II overviews the system. Section III discusses the IC design. Section IV presents experimental results.

II. System Overview

The NMR system (see Fig. 1) consists of a NdFeB Halbach permanent magnet ($B_0 = 0.51$ T and $f_0 \approx 21.8$ MHz), a solenoidal sample coil (also called RF coil) to generate RF magnetic fields and to pick up precession signals, and a CMOS RF transceiver IC. We also prepare two additional sets of coils: a shimming coil set (see Fig. 2, left) to make the static field more homogeneous for spectroscopy, and a gradient coil set (see Fig. 2, right) to introduce gradients in the static field for MRI.

The Halbach magnet has an intrinsic B_0 field inhomogeneity of 0.4 ppm (∼8.4 Hz) across a 0.8-μL sample volume at the center of the magnet bore. NMR spectroscopy, however, needs to resolve fine frequency differences around f_0 with a spectral resolution on a par with 0.1 ppm (∼2.1 Hz). To improve the homogeneity, we use the magnet with the pair of custom-designed shimming coils (see Fig. 2, left). This pair with a dc current in each generates a particular static magnetic field pattern that compensates for the B_0 inhomogeneity of the magnet [24], [27], [28], [29]. To further improve the homogeneity, we rotate the sample tube at 33 Hz, with the consequent motional averaging effectively reducing the field inhomogeneity across the plane perpendicular to the rotation axis [24], [30]. These two measures improve the B_0 field

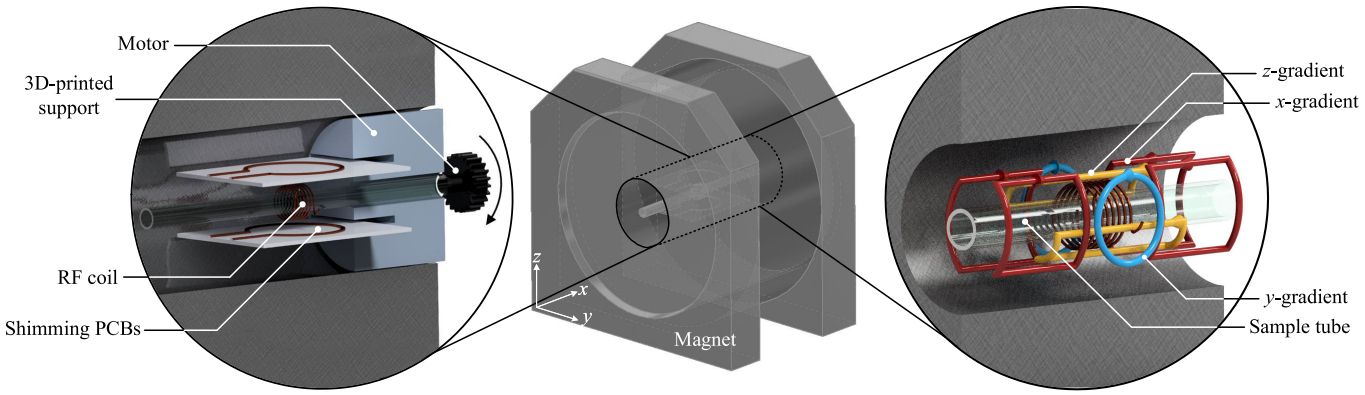

Fig. 2. For high-resolution NMR spectroscopy (left), shimming coils and motional averaging are used. For MRI (right), gradient coils are used. NMR relaxometry is performed with no shimming coils, no motional averaging, and no gradient coils.

inhomogeneity from 0.4 ppm (∼8.4 Hz) across a 0.8-μL sample to 0.05 ppm (∼1.1 Hz) across an even larger 1.4-μL sample (length of the RF coil: 1.8 mm; the inner diameter of the PTFE capillary sample tube: 1 mm). On the other hand, the intrinsic field homogeneity of the magnet is sufficient for NMR relaxometry with neither shimming nor motional averaging. In fact, we use a larger sample volume of 3.9 μL (length of the RF coil: 5 mm; the inner diameter of the tube: 1 mm) for relaxometry.

For MRI (see Fig. 2, right), samples with a volume up to ∼200 μL (RF coil length: 10 mm; sample tube inner diameter: 5 mm) can be used. To introduce gradients to the static field B_0, the sample tube with the RF coil is surrounded by three pairs of gradient coils that generate the field gradients along x-, y-, and z-directions: a Golay coil pair, a Maxwell coil pair, and a Saddle coil pair (see Fig. 2, right, red, blue, and yellow, respectively). These gradient coil pairs (as well as the shimming coils) are designed with an aid of COMSOL simulations and also based on the static magnetic field profile measured inside the magnet bore.

The CMOS transceiver IC operates the entire system. For excitation, it sends out an RF current to the sample coil to generate an RF magnetic field (in practice, a sequence of RF magnetic fields, known as RF pulse sequence, is often needed to manipulate the proton spins, and the IC is in charge of such sequence generation as well). For readout, the IC amplifies and processes precession signals to obtain spectral, relaxation, or image information. The IC also contains the electronics to control the field gradients for MRI. Section III describes the details of the IC design.

III. Design of the CMOS RF Transceiver IC

The RF transceiver IC is implemented in a standard 0.18-μm CMOS technology (while bipolar and BiCMOS technologies can be superior in speed, noise, and gain performances, the CMOS technology still allows for meeting performance requirements while offering cost competitiveness). Fig. 3 shows its architecture. Within an area of 2.34 × 2.13 mm, it integrates an RF receiver, an RF transmitter (aided by a multiphase generator), a 3-D-gradient control, and a digital control center that coordinates the operational timings of the building blocks for the NMR experiments. A supply voltage of 3.3 V is used across the chip, except the digital control center, for which a 1.8-V supply voltage is used.

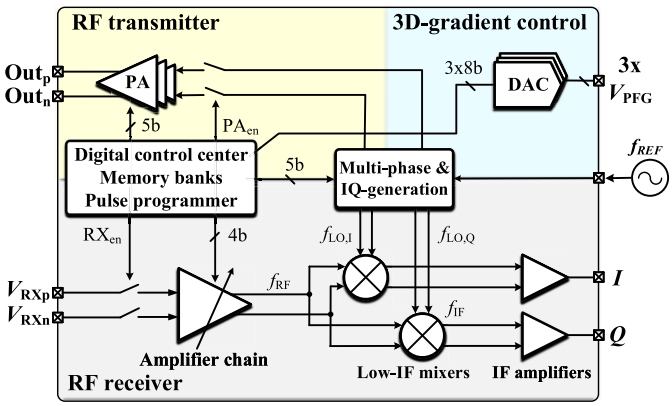

Fig. 3. Architecture of the CMOS RF transceiver IC.

A. RF Receiver

The RF receiver, which detects the RF voltage induced across the sample coil by the precession of proton spins at around $f_0 \approx 21.8$ MHz, has the heterodyne architecture (see Fig. 3). Concretely, it comprises an amplifier chain—the first stage low-noise amplifier (LNA), the second stage amplifier, and the third stage attenuator—followed by quadrature mixers for frequency down-conversion and IF-amplifiers with low-pass filter characteristics (see Figs. 3 and 4). Since our multimodal system must work with smaller samples for spectroscopy and larger samples for relaxometry and MRI, the RF input voltage to the receiver assumes a broad dynamic range, with the minimum around ∼0.6 μV for the smallest sample we use. Therefore, both the sensitivity and the ability to handle the large input dynamic range with no saturation are critical for the receiver.

For the sensitivity, to guarantee a signal-to-noise ratio (SNR) of at least 3 for the minimum input voltage of ∼0.6 μV at the receiver input, the receiver input-referred noise should be less than ∼1.2 nV/$\sqrt{\text{Hz}}$ (the relevant bandwidth for the RF input signal around f_0 used for this calculation is 30 kHz, as the IF-amplifier low-pass filters the down-converted signal

with that bandwidth). This requirement is to be met by minimizing the input-referred noise of the front-end LNA, which dominates the receiver input-referred noise. On the other hand, to accommodate the large input dynamic range with no saturation, we make the voltage gain of the entire receiver chain tunable between 34 and 100 dB. Specifically, the gains of the first-stage LNA and the second-stage amplifier are 26 and 20 dB, respectively; the third-stage programmable attenuator has a gain that can be tuned from −66 to 0 dB; and the quadrature mixers and IF-amplifiers together offer an additional gain of 54 dB. For a larger input voltage, we use a larger attenuation in the third stage attenuator so that the mixers and IF-amplifiers are not saturated (the first-stage LNA and the second-stage amplifier are not saturated for the range of sample volumes we use). In addition, to make the IC usable not only at room temperature but also at higher temperatures for such applications as subsurface oil exploration, we endeavor to make the IC—in particular, the receiver that can be especially temperature sensitive—operate up to 125 °C with temperature-compensated design.

The LNA (see Fig. 4) in a differential form, which interfaces with the coil, uses resistive loads and pMOS input transistors M_1 and M_2 whose $1/f$ noise corner (<1 MHz) is far below $f_0 \approx 21.8$ MHz. To minimize thermal noise, we increase the transconductance g_m of the input transistors using larger channel widths and also by increasing their bias currents within a power budget. At the same time, the LNA gain is made temperature-insensitive to the first order, following the recipe from our previous work [23]. A standard analysis of the bottom part of the biasing circuit formed by transistors M_3 and M_4 in the pinch-off regime and resistor R_b (see Fig. 4, left) yields a bias current $I_b = [2\mu_n C_{ox}(W/L)_4 R_b^2]^{-1}$ where μ_n is the electron mobility, C_{ox} is the gate oxide capacitance per unit area, and $(W/L)_4$ is the channel width-to-length ratio of M_4. Or by considering only the temperature-dependent parameters, $I_b \propto \mu_n^{-1} R_b^{-2}$. Since I_b is mirrored to the LNA, g_m of M_1 or M_2 of the LNA is then expressed as $g_m \propto 1/R_b \times (\mu_p/\mu_n)^{1/2}$, again including only the temperature-dependent parameters, where μ_p is the hole mobility. Approximating that μ_p and μ_n have the same temperature dependency, the voltage gain of the LNA is then given by $g_m R_1 \propto R_1/R_b$, where R_1 is the load resistor of the LNA. Since both resistors R_1 and R_b have the same temperature dependency, the LNA gain is temperature-insensitive to the first order. The same scheme also applies to the second-stage amplifier (see Fig. 4).

The third-stage programmable attenuator is controlled with a 4-bit digital signal. It is a 12-step R-$2R$ resistor ladder with an attenuation of 6 dB per step, and the attenuation thus can be tuned from 0 to 66 dB. The noise from this resistive network is rather negligible due to the considerable amplification by the first two stages. The attenuation level is stored in a global configuration register memory bank.

The output of the amplifier chain is then frequency down-converted by mixers driven by quadrature local oscillator signals and low-pass filtered by IF-amplifiers, resulting in the final receiver outputs, I and Q, at audio frequencies. The I and Q signals contain frequency and phase information on the proton spin precession, from which spectral, relaxation, or imaging information can be extracted.

B. RF Transmitter Aided by Multiphase Generator

The RF transmitter drives the sample coil with an RF output current at the resonant frequency $f_0 \approx 21.8$ MHz to produce an RF magnetic field with an amplitude B_1 inside the coil. This field will tilt $\vec{\mu}$ away from the B_0 direction, increasing the angle between them, thus increasing the energy of proton spins. The final excitation angle at the end of the duration Δt of the RF current application is $\theta = \gamma(B_1/2)\Delta t$, where B_1 is proportional to the RF current amplitude for a given sample coil. At the same time, the phase of the RF excitation—e.g., whether the RF magnetic field is $B_1 \sin(2\pi f_0 t)$ or $B_1 \cos(2\pi f_0 t)$ or any other phase—determines the direction $\vec{\mu}$ is tilted away. Therefore, if the amplitude, phase, and duration of the RF current are tunable, one can control the $\vec{\mu}$ excitation in a versatile manner. Our RF transmitter is built in such a way that all three parameters are tunable. Specifically, it is built by combining a digitally controlled current mode class-D power amplifier (PA) and a multiphase generator based on a delay-locked loop (DLL) (see Figs. 5 and 6).

The tuning of the RF current amplitude is achieved by building the PA with 31 identical unit amplifiers in parallel (see Fig. 5). Each unit amplifier stacks two nMOS-transistors. The bottom transistor functions as a current source driven by a fixed-amplitude RF input signal arriving from the multiphase generator with a selected phase. The top transistor acts as a switch. As the voltage of the drain node of the top transistor can be as high as πV_{DD} [31], we use thick-oxide options for both transistors available in the CMOS technology with a drain breakdown voltage in excess of 12 V. The output RF current amplitude of the PA is tuned by choosing the number of unit amplifiers to activate. Using a 31-bit thermometer code to choose unit amplifiers to activate, we make available 32 discrete RF current amplitudes, with the lowest being zero with all unit amplifiers deactivated and the highest being ~300 mA with all unit amplifiers activated. These 32 current amplitudes in combination with the tunable excitation duration, $1\ \mu s \leq \Delta t \leq 200\ \mu s$ (the Δt tuning is done simply by controlling the time to activate and deactivate the PA with the thermometer code), are sufficient to control $\theta = \gamma(B_1/2)\Delta t$ to any desired value for a broad range of sample volumes used in our multimodal system operation (the proportionality of the RF current amplitude to B_1 varies with the sample coil diameter). Since the output impedance of the PA decreases with an increasing number of activated unit amplifiers, the PA output current will not perfectly linearly scale with the thermometer code. This nonlinearity, however, is not an issue in our system operation, because for each excitation, we always use a constant RF output current amplitude (a constant thermometer code) we choose from the 32 options.

The tuning of the RF current phase is achieved using the multiphase generator based on a DLL (see Fig. 6), similar to the one used in one of our previous works [23]. The phase frequency detector (PFD) compares the phases of the incoming RF signal and its delayed version from the tunable delay line.

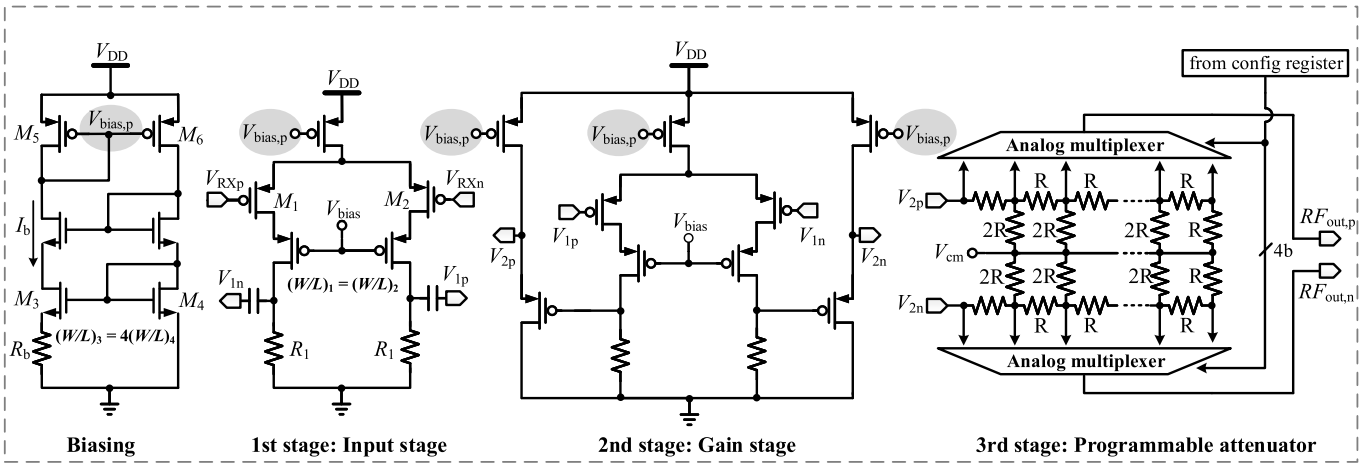

Fig. 4. Biasing circuit and first, second, and third stage of the receiver amplifier chain.

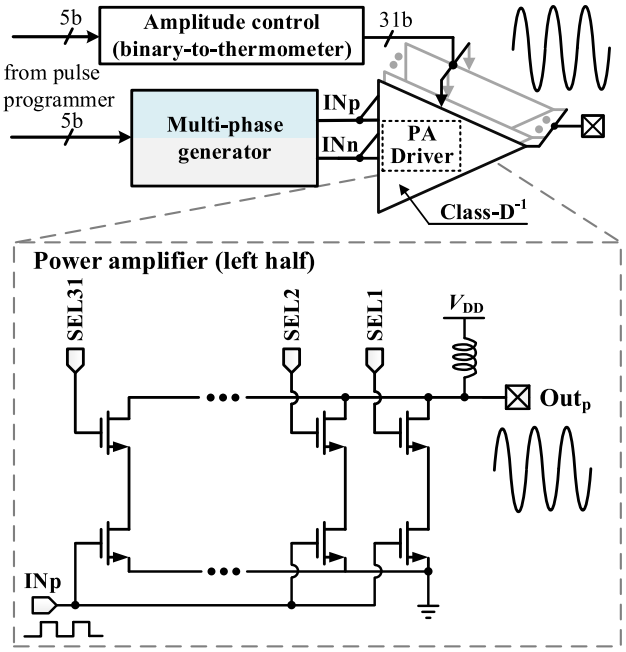

Fig. 5. RF transmitter.

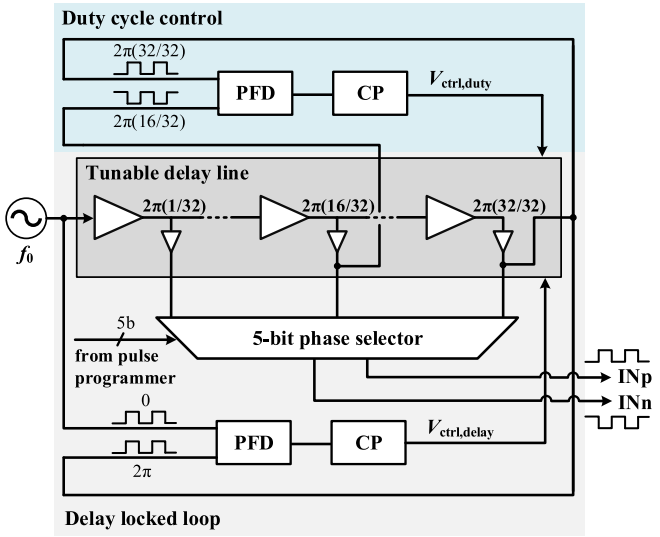

Fig. 6. DLL-based multiphase generator.

The outcome of this comparison feeds the charge pump (CP) to generate a control voltage to tune the line delay so that it is locked to one RF period, or the phase of 2π. As the delay line has 32 nodes accessible by a 5-bit phase selector, we can choose any one of 32 RF phases equally spaced between 0 and 2π (32 available phases are sufficient for most NMR experiments in practice). The output of the DLL, IN_p (and its inverted version IN_n) with the selected phase is what drives the PA. For maximum PA efficiency, a 50% duty cycle for IN_p is desired, but due to different rise and fall times of the cells in the delay line, the duty cycle may deviate from 50%. To address this issue, we add an auxiliary feedback loop (see Fig. 6, blue), which compares the RF signals from the 16th and 32nd nodes of the delay line and adjust the rise and fall characteristics of the delay line until the 50% duty cycle is achieved, upon which the two signals become accurate inversions of each other and the control voltage in the auxiliary circuit is locked.

C. Gradient Field Control for MRI

We generate static magnetic field gradients on top of B_0 along each of x-, y-, and z-directions, by injecting a current into each gradient coil pair (see Section II). Since the NMR frequency becomes then a function of position, NMR relaxometry with a fixed RF excitation frequency measures T_2 from only a small sample portion whose NMR frequencies are close enough to the excitation frequency. Thus, as we alter the field gradients by changing the amount of currents injected in the gradient coil pairs, different portions of the sample will be selected for NMR relaxometry, producing a heat map of T_2—i.e., an MRI image—across the sample region the varied field gradients can cover. The injected current in our system can be tuned from -1.5 to 1.5 A, and the corresponding range of the field gradients can scan a sample length of 6 mm. The step of the field gradient change is related to the imaging resolution, and with 256 steps of injected current change and thus with

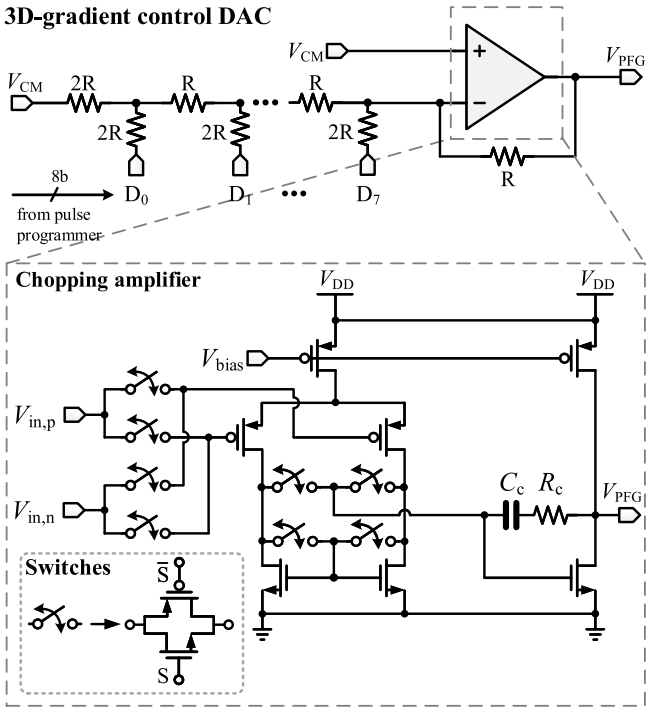

Fig. 7. Gradient control DAC with chopper-stabilized amplifier.

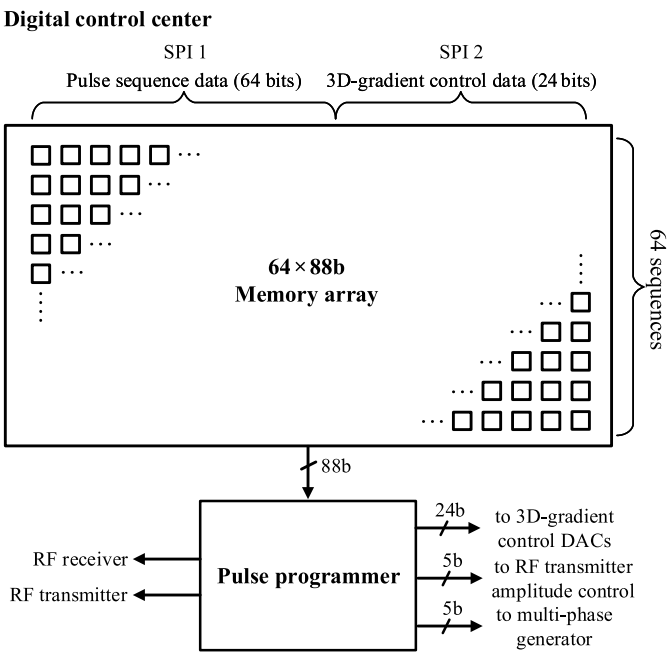

Fig. 8. Simplified architecture of the digital control center.

256 steps of field gradient change, an average target spatial resolution along the scanned length of 6 mm may be estimated as ~6 mm/256 × 2 ≈ 47 μm, where the factor 2 arises due to the technical details involved with the particular MRI algorithm we use [26].

For the 256-step current injection change, we build three 8-bit digital-to-analog converters (DACs) ON chip (see Fig. 3) for the three gradient coil pairs. The output voltage of each DAC is then converted into a current by OFF-chip electronics on a printed circuit board (PCB), as the current as large as ±1.5 A ON chip could cause heating and electromigration. The PCB contains π-filters, buffer stages, and high-power op-amps for voltage-to-current conversion.

Fig. 7 shows the schematic of each identical ON-chip DAC. It is of the R-$2R$ topology and uses a chopper-stabilized op-amp in a negative feedback loop to mitigate the offset and $1/f$ noise for high fidelity. The chopping frequency is chosen at 8 MHz, a value larger than the $1/f$ noise corners of the transistors in the op-amp, to suppress the $1/f$ noise. At the same time, the associated 8-MHz ripples interfere neither with the RF frequency (>20 MHz) nor with the down-converted IF frequency (<100 kHz) in the transceiver. The output of the DACs is low-pass filtered to minimize the ripples. To operate these DACs in harmony with the RF pulse sequences with all the relevant timings synchronized, each individual DAC is equipped with its own digital memory bank (64 × 8 bits), which is linked to the digital control center to be discussed shortly.

D. Digital Control Center

While the most basic NMR experiment involves a single RF excitation period followed by a single-precession readout period (see Section I), in many advanced and widely used NMR experiments, a sequence of excitations with tight control of excitation amplitudes, phases, and durations is intermixed with multiple spin precession periods, some of which are read-out. The sequence of excitations is called RF pulse sequence. Therefore, the operational timings of the transmitter and the receiver, as well as the phases and amplitudes of the transmitter need to be all together coordinated. In MRI, these transceiver operations need to be also properly synchronized with the operation of the gradient coils.

Such complex operation of the entire chip is managed by the digital control center (see Fig. 8), which consists of a 64 × 88-bit shift-register memory array and a pulse programmer (digital logic). The first 64 bits of each row of the memory array store largely an RF pulse sequence instruction such as the width, amplitude, and phase of each excitation RF pulse and the pause duration between adjacent excitation RF pulses, but also an instruction on the timing of the receiver operation. The remaining 24 bits of the row are divided into three 8-bit instructions for 3-D field gradient control (this portion is relevant only when the system is engaged in MRI). The instruction of each row is then translated by the pulse programmer to control the transmitter together with the multiphase generator, the receiver, and the three DACs. The digital control center runs with a 16-MHz clock. The memory array is programed via two serial peripheral interfaces (SPIs), one for the first 64 bits of each row (pulse sequence instruction), and the other for the remaining 24 bits of the row (MRI field gradient instruction). Of note, the digital control center also includes a separate 64-bit configuration register (not shown in Fig. 8) to store frequently used data such as the target receiver gain; this arrangement streamlines I/O's and reduces external auxiliary circuits.

Furthermore, an NMR pulse sequence can contain a great number of repeated excitation pulses, which may not be possible to put into the shift register memory array. We overcome this issue by providing three execution loops in the pulse programmer. These loops can be used independently, or in a nested manner, allowing for a much simpler instruction stored in the memory array.

IV. Experiments

A. IC Characterization

Before conducting NMR experiments, we characterize the CMOS RF transceiver IC with $f_0 \approx 21.8$ MHz. The measured tuning range of the voltage gain of the RF receiver is 30–100 dB, which exceeds the simulated range of 34–100 dB. The input-referred noise of the receiver is 0.78 nV/$\sqrt{\text{Hz}}$, which is obtained by first measuring the output voltage noise with the input voltage terminals shortcircuited, and then dividing it by the maximum voltage gain measured (100 dB). We also use the procedure in [32] to measure the amplitude mismatch of ~0.1 dB between the I and Q channels and the maximum ~1.7 °C error in reference to 90 °C in the phase difference between the I and Q channels. The receiver dissipates a maximum power of 43 mW from the 3.3 V supply.

Fig. 9(a), left, shows that the receiver gain drops only by ~3 dB as temperature increases from 20 °C to 125 °C with the chip placed in a temperature chamber. Our attention to temperature sensitivity arises because we seek to use the IC not only at room temperature but also for subsurface exploration where temperature is high (see Section III). Since the supply voltage provided by OFF-chip power regulators can vary with temperature, we also measure the receiver gain for supply voltages varied up to ±10% around 3.3 V; the receiver gain then varies only by ±1 dB (see Fig. 9(a), right). Both measurements in Fig. 9(a) agree well with post-layout simulations.

The amplitude of the RF output current of the transmitter into a 1-Ω load is tuned from 25 to ~290 mA [see Fig. 9(b)], as we activate more unit amplifiers. The nonlinearity seen arises because the PA's output impedance decreases as more unit amplifiers are activated. As discussed in Section III, this nonlinearity is not an issue in our NMR operation. Finally, to a matched load (4.9 Ω), the transmitter delivers a maximum output power of 220 mW, while consuming a maximum power of 560 mW from the 3.3 V supply.

Fig. 9(c) shows the measured DAC output voltage—from each of the three gradient control DACs—which is apparently varied linearly from 0 to 3.3 V with the digital code. The figure also displays the OFF-chip conversion of one of the DAC output voltages into a current (+1.5 to −1.5 A) to drive a gradient coil pair. Fig. 9(d) shows the measured differential and integral nonlinearities (DNL and INL) of a DAC, which are within ±0.23 LSB and −0.36/0.24 LSB, respectively. The three DACs together consume a maximum power of ~2 mW from the 3.3 V supply. Digital circuits on the chip dissipate a power less than 1 mW from the 1.8 V supply.

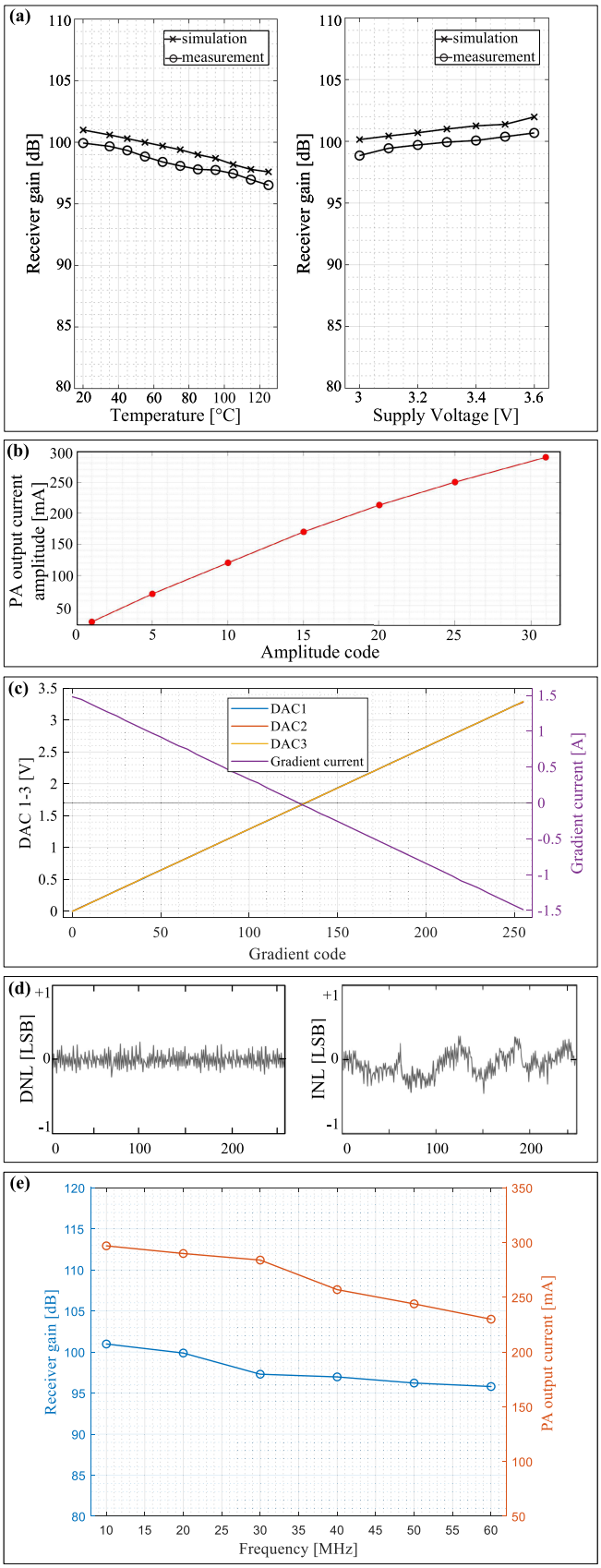

Fig. 9. IC measurements: (a) RF receiver gain versus temperature and supply voltage. (b) RF transmitter output current amplitude (1-Ω load) versus number of activated unit amplifiers. (c) DAC output voltages and OFF-chip converted current. (d) DAC DNL and INL. (e) RF receiver gain and RF transmitter output current amplitude for a range of frequencies.

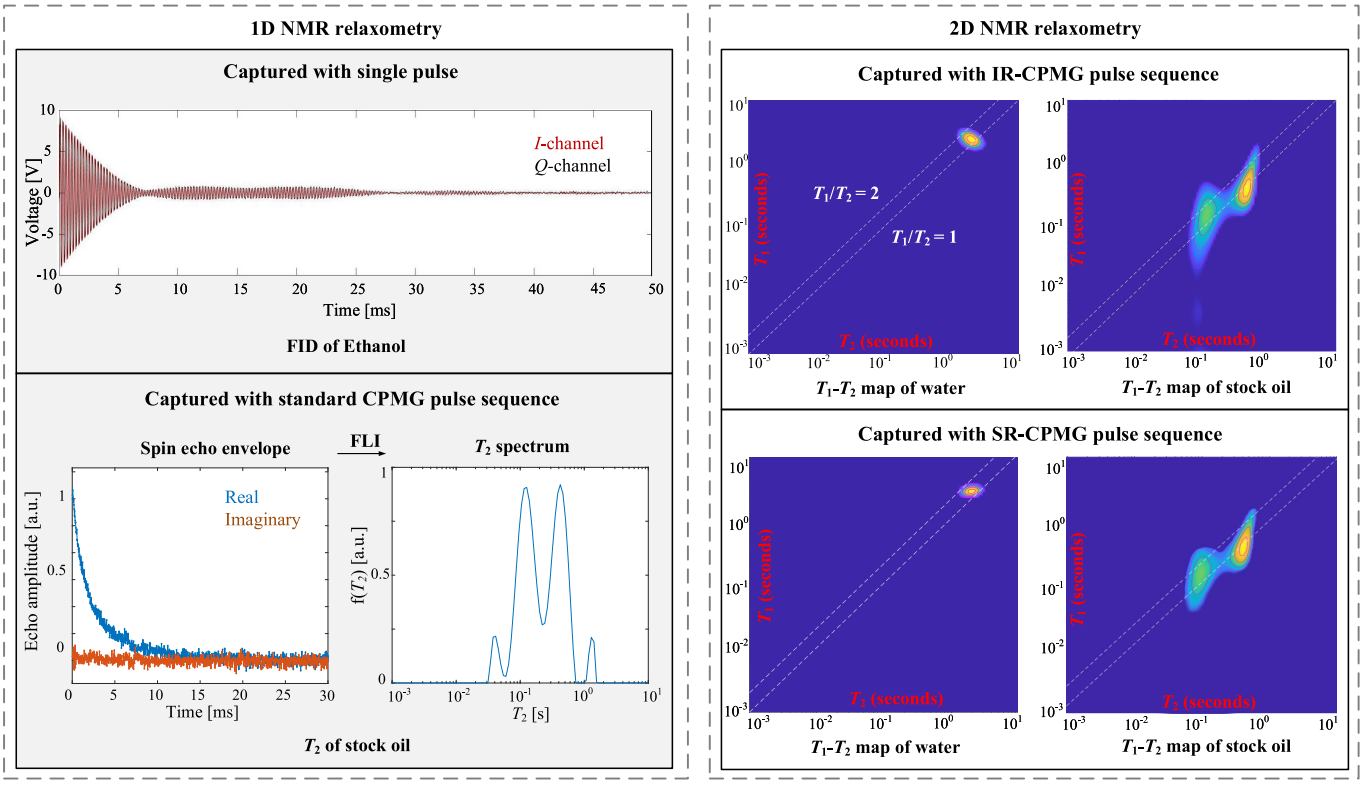

Fig. 10. One-dimensional and 2-D NMR relaxometry measurement results. One-dimensional: FID of Ethanol, captured after single pulse excitation (top-left), and T_2 measurement of stock oil, captured with standard CPMG (bottom-left). Two-dimensional: T_1-T_2 maps of water and stock oil captured with IR-CPMG (top-right), and SR-CPMG (bottom-right), enabled by the ON-chip nested loop feature.

Finally, Fig. 9(e) shows the receiver gain and the transmitter RF output current amplitude over a broad range of RF frequencies. While our focus in this article is ^{1}H NMR at $f_0 \sim 21$ MHz with $B_0 \sim 0.5$ T, given the transceiver capability over the broader frequency range shown in the figure, the chip may be used for a broader range of B_0 and with other NMR active nuclei.

B. NMR Relaxometry

Ideally T_2 (the characteristic damping time of the precession signal due primarily to phase decoherence; Section I) can be obtained from the precession signal after a single excitation. The damping of such a precession signal, called free induction decay (FID), however, includes the dephasing effects due not only to the sample itself (which we seek to interrogate) but also to the B_0 inhomogeneity (which is an artifact). This is overcome by the RF pulse sequence known as Carr–Purcell–Meiboom–Gill (CPMG) sequence, which includes multiple excitations with a particular set of excitation durations and intervals, with which precession signals repeat to appear and disappear. The envelope of such "spin echo" decays, capturing the true T_2 due only to the sample, with the B_0 inhomogeneity effect removed. Fig. 10, top-left and bottom-left, show the FID of ethanol and the spin echo decay of a stock oil, respectively, both after frequency-down conversion. In Fig. 10, bottom-left, a fast Laplace inversion of the echo signal reveals multiple T_2 values, typical of oil containing hydrocarbon molecules with differing sizes.

The measurement of T_1, the characteristic damping time due purely to energy loss (i.e., the characteristic time for an excited μ to align back to B_0), involves a more complex RF pulse sequence scheme. In fact, we can measure both T_1 and T_2 with RF pulse sequence schemes known as inversion-recovery-CPMG (IR-CPMG) and saturation-recovery CPMG (SR-CPMG). Fig. 10, top-right and bottom-right, show T_1-T_2 maps of tap water and stock oil, measured with the IR-CPMG and SR-CPMG sequences, respectively. Both sequence schemes reveal essentially identical T_1-T_2 map features: the single, tight peaks for water are due to the rapidly rotating water molecules, while the broader distributions for oil reflect more complex interactions among hydrocarbon molecules of varying sizes. The SR-CPMG scheme is faster in experiments than the IR-CPMG scheme but is also more complex. Its execution is greatly facilitated by the loop feature of the pulse programmer in the digital control center.

C. NMR Spectroscopy

We perform high-resolution NMR spectroscopy with the custom-designed shimming coils and motional averaging (see Section II). Fig. 11, left, shows the ^{1}H NMR spectrum obtained from an ethyl acetate sample. With a spectral resolution of 0.05 ppm (for $f_0 \approx 21.8$ MHz, this corresponds to a frequency resolution of 1.1 Hz; this is the highest resolution achieved by a portable CMOS-based NMR system based on a permanent magnet), all the known spectral peaks (corresponding to chemical shifts and J-coupled splittings) around f_0 due to

TABLE I
COMPARISON WITH RECENT CMOS-BASED MAGNETIC RESONANCE SYSTEMS

Specifications	**This work**	[26] S. Fan *JSSC'22*	[24] K.-M. Lei *Anal. Chem.'20*	[39] J. Handwerker *Nat. Methods'20*	[36] Q. Yang *Magn. Reson.'22*	[37] F. Dreyer *NEWCAS'22*	[38] F. Dreyer *BioCAS'22*
System Performance							
Functionality	**NMR Relaxometry NMR Spectroscopy MRI**	NMR Relaxometry MRI	NMR Relaxometry NMR Spectroscopy MRI	NMR Relaxometry NMR Spectroscopy MRI	NMR Relaxometry NMR Spectroscopy	NMR Spectroscopy	NMR Relaxometry
Magnet	**Permanent (0.51 T)**	Permanent (0.52 T)	Permanent (0.51 T)	Superconducting (14.1 T)	Permanent (0.36 T)	Permanent (1.45 T)	Permanent (0.36 T)
Imaging	**On-Chip**	On-Chip	Off-Chip	Off-Chip	N/A	N/A	N/A
Spin sensitivity† [spins/√Hz•T²/m]	**2.1×10^{15}**	N/A	N/A	2.4×10^{22}	1.7×10^{20}	8.3×10^{17}	4.6×10^{15}
Circuit Performance							
Technology	**0.18 µm CMOS**	0.18 µm HV-CMOS SOI	0.18 µm CMOS	0.18 µm CMOS	0.13 µm BiCMOS	0.13 µm BiCMOS	0.13 µm BiCMOS
Frequency Range [MHz]	**10-60**	22.2	10-40	600	5.7-770	5-780	N/A
Input-referred noise [nV/√Hz]	**0.78**	0.89 (0.63*)	0.82	1.26	0.77	0.61	0.61
Gain [dB]	**30-100**	85.2	34-100	N/A	45-85	31.5-66	N/A
PA I_{out} [mA]⁺	**290**	602	251	N/A	90	105	200ˣ
On-chip transmitter AM/PM	**Yes**	Yes	Yes	No	No	No	No
Area (mm²)	**5**	6	4	1.8	1	1	1

*after software-domain signal processing ⁺1-Ω load ˣtuned RF coil †normalized: $N_{min,n}=N_{min}\times B_0^2/d_{coil}$

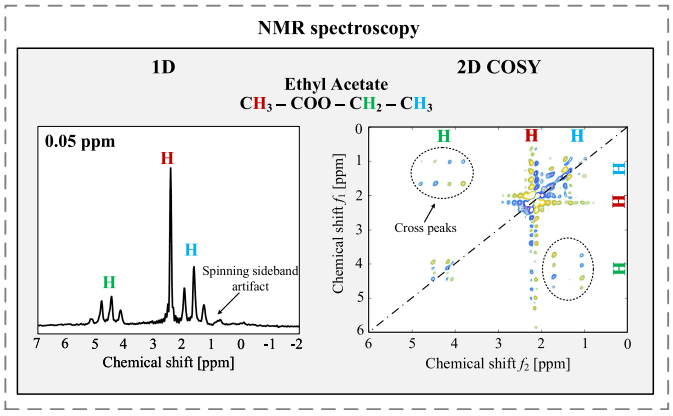

Fig. 11. One-dimensional and 2-D NMR spectroscopy results. One-dimensional: measurements on ethyl acetate showing the importance of a high-resolution (left). Two-dimensional: ^{1}H–^{1}H COSY on ethyl acetate (right).

the molecular structure are observed [33]. This spectrum is obtained by averaging 16 scans, and the drift of B_0 from the permanent magnet due to temperature fluctuation during the scans is calibrated out [23]. The absolute and normalized spin sensitivities [34], [35] are 1.4×10^{13} spins/$\sqrt{\text{Hz}}$ and 2.1×10^{15} spins/$\sqrt{\text{Hz}} \times \text{T}^2/\text{m}$.

We also perform 2-D NMR spectroscopy, a technique that transformed the field of NMR with the power to greatly facilitate the molecular structure determination. In particular, we perform correlation spectroscopy (COSY) on ethyl acetate, where COSY is one of the most widely used 2-D NMR spectroscopy techniques. It involves an execution of multiple (808 in our specific experiment) RF pulse sequences with two-time parameters. The appreciable B_0 drift caused by temperature fluctuation during the inherently long experiment is calibrated out. Fig. 11, right, shows the COSY NMR spectrum so obtained for ethyl acetate. It is spread out in two dimensions of frequencies. While the diagonal peaks are suboptimal, the OFF-diagonal cross peaks, which are of paramount importance in COSY, are clearly resolved, directly revealing which groups of ^1H protons in the molecule are coupled to which other groups [33].

D. Magnetic Resonance Imaging

For MRI, we activate the ON-chip gradient control. The field of view is 6 mm and field gradients are increased up to 200 mT/m. For imaging, we use the RF pulse sequence and the gradient field control sequences shown in Fig. 12, top: in the figure, the 90° and 180° pulses mean excitation RF fields that are sustained to tilt $\vec{\mu}$ by 90° and by 180°, respectively. To acquire the image, the gradient control sequences (with the same RF pulse sequence) need to be repeated with the gradients varied. In this way, we image a yz cross section of a 5-mm tube, a xz cross section of a 3-mm tube (see Fig. 12, middle), and a 3-D-printed alphabet groove (letter "V"), all filled with water containing ^{1}H proton spins (see Fig. 12, bottom). The spatial imaging resolution is $67 \times 67 \times 83$ μm^3.

E. Comparison

Table I compares our system, which combines multidimensional NMR relaxometry, high-resolution NMR spectroscopy,

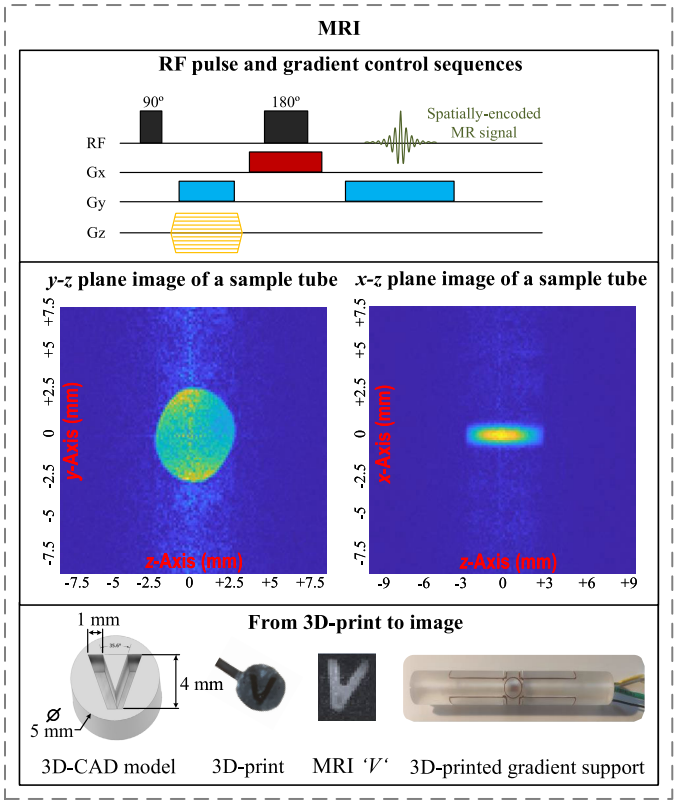

Fig. 12. MRI results. RF pulse and gradient control sequences used for capturing the images (top), images of a 5- and 3-mm sample tube, validating the 3-D-MRI functionality (center), along with a 2-D-image of a 3-D-printed alphabet phantom (bottom).

and MRI in a single, portable platform, with recent CMOS- and BiCMOS-based NMR systems. Yang et al. [36] and Dreyer et al. [37], [38] are limited to NMR relaxometry and/or spectroscopy. Lei et al. [26], Fan et al. [24], and Handwerker et al. [39] include MRI, but [26] lacks spectroscopy capabilities, [24] uses OFF-chip gradient control, and [39] relies on a superconducting magnet.

V. Conclusion

We have presented a portable NMR platform capable of all three key NMR modalities: multidimensional NMR relaxometry, high-resolution NMR spectroscopy, and MRI. It achieves not only a state-of-the-art spectral resolution of <0.05 ppm—the highest resolution reported for portable CMOS-based systems based on permanent magnets—for NMR spectroscopy, but also a spatial resolution of $67 \times 67 \times 83$ μm^3 for MRI. This advance of the multimodal NMR platform is attributed not only to the overall instrument engineering, but also to the design of the digitally assisted CMOS RF transceiver IC that meets complex RF, mixed-mode, and digital requirements.

From a broader point of view, recent years have witnessed prodigious efforts to interface CMOS chips with biological and chemical systems: e.g., CMOS ion-sensitive field-effect transistor arrays for DNA sequencing [40], CMOS electrochemical cell arrays for DNA synthesis [41], and CMOS nanoelectrode arrays for intracellular neuronal recording [42], [43]. CMOS-based NMR may be viewed as what lies along this line of effort that interfaces CMOS electronics with material systems for life science, chemistry, and material science applications.

Acknowledgment

The authors thank Dr. Isik Kizilyalli, Program Director of the Advanced Research Projects Agency-Energy (ARPA-E).

References

[1] J. D. Roberts, *Nuclear Magnetic Resonance: Applications to Organic Chemistry*. New York, NY, USA: McGraw-Hill, 1959.
[2] W. P. Aue, E. Bartholdi, and R. R. Ernst, "Two-dimensional spectroscopy. Application to nuclear magnetic resonance," *J. Chem. Phys.*, vol. 64, no. 5, pp. 2229–2246, 1976.
[3] K. Wüthrich, "NMR with proteins and nucleic acids," *Europhys. News*, vol. 17, no. 1, pp. 11–13, 1986.
[4] P. Mansfield and A. A. Maudsley, "Medical imaging by NMR," *Brit. J. Radiol.*, vol. 50, no. 591, pp. 188–194, Mar. 1977.
[5] E. R. Andrew, "A historical review of NMR and its clinical applications," *Brit. Med. Bull.*, vol. 40, no. 2, pp. 115–119, 1984.
[6] Z.-P. Liang and P. C. Lauterbur, *Principles of Magnetic Resonance Imaging*. Bellingham, WA, USA: SPIE, 2000.
[7] K. Wüthrich, "The way to NMR structures of proteins," *Nature structural Biol.*, vol. 8, no. 11, pp. 923–925, 2001.
[8] K.-J. Dunn, D. J. Bergman, and G. A. LaTorraca, *Nuclear Magnetic Resonance: Petrophysical and Logging Applications*. Amsterdam, The Netherlands: Elsevier, 2002.
[9] M. D. Hürlimann, "Well logging," in *eMagRes*. Hoboken, NJ, USA: Wiley, 2012. [Online]. Available: https://onlinelibrary.wiley.com/doi/abs/10.1002/9780470034590.emrstm0593.pub2, doi: 10.1002/9780470034590.emrstm0593.pub2.
[10] I. I. Rabi, J. R. Zacharias, S. Millman, and P. Kusch, "A new method of measuring nuclear magnetic moment," *Phys. Rev.*, vol. 53, no. 4, p. 318, Feb. 1938.
[11] F. Bloch, "Nuclear induction," *Phys. Rev.*, vol. 70, nos. 7–8, pp. 460–474, Oct. 1946.
[12] E. M. Purcell, H. C. Torrey, and R. V. Pound, "Resonance absorption by nuclear magnetic moments in a solid," *Phys. Rev.*, vol. 69, nos. 1–2, pp. 37–38, Jan. 1946.
[13] E. L. Hahn, "An accurate nuclear magnetic resonance method for measuring spin-lattice relaxation times," *Phys. Rev.*, vol. 76, no. 1, pp. 145–146, Jul. 1949.
[14] N. Arunkumar et al., "Quantum logic enhanced sensing in solid-state spin ensembles," 2022, *arXiv:2203.12501*.
[15] J. Weis and A. H. Velders, "Nuclear magnetic resonance on a chip," *Lab Chip*, vol. 14, no. 6, pp. 959–980, 2014.
[16] J. Anders, F. Dreyer, D. Krüger, I. Schwartz, M. B. Plenio, and F. Jelezko, "Progress in miniaturization and low-field nuclear magnetic resonance," *J. Magn. Reson.*, vol. 322, Jan. 2021, Art. no. 106860.
[17] S. Fan, Q. Zhou, K.-M. Lei, P.-I. Mak, and R. P. Martins, "Miniaturization of a nuclear magnetic resonance system: Architecture and design considerations of transceiver integrated circuits," *IEEE Trans. Circuits Syst. I, Reg. Papers*, vol. 69, no. 8, pp. 3049–3060, Aug. 2022.
[18] Y. Liu, N. Sun, H. Lee, R. Weissleder, and D. Ham, "CMOS mini nuclear magnetic resonance system and its application for biomolecular sensing," in *IEEE Int. Solid-State Circuits Conf. (ISSCC) Dig. Tech. Papers*, Feb. 2008, pp. 140–141.
[19] N. Sun, Y. Liu, H. Lee, R. Weissleder, and D. Ham, "CMOS RF biosensor utilizing nuclear magnetic resonance," *IEEE J. Solid-State Circuits*, vol. 44, no. 5, pp. 1629–1643, May 2009.
[20] N. Sun et al., "Palm NMR and one-chip NMR," in *IEEE Int. Solid-State Circuits Conf. (ISSCC) Dig. Tech. Papers*, Feb. 2010, pp. 488–489.
[21] N. Sun, T.-J. Yoon, H. Lee, W. Andress, R. Weissleder, and D. Ham, "Palm NMR and 1-Chip NMR," *IEEE J. Solid-State Circuits*, vol. 46, no. 1, pp. 342–352, Jan. 2011.
[22] N. Sun, Y. Liu, L. Qin, H. Lee, R. Weissleder, and D. Ham, "Small NMR biomolecular sensors," *Solid-State Electron.*, vol. 84, pp. 13–21, Jun. 2013.
[23] D. Ha, J. Paulsen, N. Sun, Y.-Q. Song, and D. Ham, "Scalable NMR spectroscopy with semiconductor chips," *Proc. Nat. Acad. Sci. USA*, vol. 111, no. 33, pp. 11955–11960, Aug. 2014.
[24] K.-M. Lei et al., "Portable NMR with parallelism," *Anal. Chem.*, vol. 92, no. 2, pp. 2112–2120, Jan. 2020.
[25] D. Kruger et al., "A portable CMOS-based MRI system with $67\times67\times83$ μm^3 image resolution," in *Proc. ESSCIRC IEEE 48th Eur. Solid State Circuits Conf. (ESSCIRC)*, Sep. 2022, pp. 225–228.

[26] S. Fan, Q. Zhou, K.-M. Lei, P.-I. Mak, and R. P. Martins, "A miniaturized 3-D-MRI scanner featuring an HV-SOI ASIC and achieving a 10 × 8 × 8 mm^3 field of view," *IEEE J. Solid-State Circuits*, early access, Dec. 5, 2022, doi: 10.1109/JSSC.2022.3223215.
[27] M. Weiger, D. Moskau, R. Kerssbaum, and W. Hull, "Gradient shimming: Principles and practical aspects," *Bruker SpinReport*, vol. 158, pp. 1–37, 01 2007.
[28] M. Weiger and T. Speck, "Shimming for high-resolution NMR spectroscopy," in *eMagRes*. Hoboken, NJ, USA: Wiley, 2011. [Online]. Available: https://onlinelibrary.wiley.com/doi/abs/10.1002/9780470034590.emrstm1228, doi: 10.1002/9780470034590.emrstm1228.
[29] M. Blasche and D. Fischer, "Magnet homogeneity and shimming," in *Siemens Healthineers*. Erlangen, Germany: Siemens Healthcare GmbH, 2017.
[30] H. Günther, *NMR Spectroscopy: Basic Principles, Concepts and Applications in Chemistry*. Hoboken, NJ, USA: Wiley, 2013.
[31] H. Kobayashi, J. M. Hinrichs, and P. M. Asbeck, "Current-mode class-D power amplifiers for high-efficiency RF applications," *IEEE Trans. Microw. Theory Techn.*, vol. 49, no. 12, pp. 2480–2485, Dec. 2001.
[32] J. Anders, P. SanGiorgio, and G. Boero, "A quadrature receiver for μNMR applications in 0.13 μm CMOS," in *Proc. ESSCIRC*, Sep. 2010, pp. 394–397.
[33] M. Balci, *Basic 1H-and 13C-NMR Spectroscopy*. Amsterdam, The Netherlands: Elsevier, 2005.
[34] J. Anders, J. Korvink, O. Brand, G. Fedder, C. Hierold, and O. Tabata, *Micro and Nano Scale NMR: Technologies and Systems* (Advanced Micro and Nanosystems). Hoboken, NJ, USA: Wiley, 2018. [Online]. Available: https://books.google.de/books?id=GVZaDwAAQBAJ
[35] H. Bürkle, K. Schmid, T. Klotz, R. Krapf, and J. Anders, "A high voltage CMOS transceiver for low-field NMR with a maximum output current of 1.4 A_{pp}," in *Proc. IEEE Int. Symp. Circuits Syst. (ISCAS)*, Oct. 2020, pp. 1–5.
[36] Q. Yang, J. Zhao, F. Dreyer, D. Krüger, and J. Anders, "A portable NMR platform with arbitrary phase control and temperature compensation," *Magn. Reson.*, vol. 3, no. 1, pp. 77–90, May 2022. [Online]. Available: https://mr.copernicus.org/articles/3/77/2022/
[37] F. Dreyer, D. Kruger, S. Baas, A. Velders, and J. Anders, "A broadband transceiver ASIC for X-nuclei NMR spectroscopy in 0.13 μm BiCMOS," in *Proc. 20th IEEE Interregional NEWCAS Conf. (NEWCAS)*, Jun. 2022, pp. 65–69.
[38] F. Dreyer, Q. Yang, D. Kruger, and J. Anders, "A chip-based NMR relaxometry system for point-of-care analysis," in *Proc. IEEE Biomed. Circuits Syst. Conf. (BioCAS)*, Oct. 2022, pp. 183–187.
[39] J. Handwerker et al., "A CMOS NMR needle for probing brain physiology with high spatial and temporal resolution," *Nature Methods*, vol. 17, no. 1, pp. 64–67, Jan. 2020.
[40] J. M. Rothberg, W. Hinz, and J. Bustillo, "An integrated semiconductor device enabling non-optical genome sequencing," *Nature*, vol. 475, no. 7356, pp. 348–352, 2011.
[41] H. S. Jung et al., "CMOS electrochemical pH localizer-imager," *Sci. Adv.*, vol. 8, no. 30, Jul. 2022, Art. no. eabm6815.
[42] J. Abbott et al., "A nanoelectrode array for obtaining intracellular recordings from thousands of connected neurons," *Nature Biomed. Eng.*, vol. 4, no. 2, pp. 232–241, Sep. 2019.
[43] D. Ham, H. Park, S. Hwang, and K. Kim, "Neuromorphic electronics based on copying and pasting the brain," *Nature Electron.*, vol. 4, no. 9, pp. 635–644, Sep. 2021.

Daniel Krüger (Graduate Student Member, IEEE) received the B.S. and M.S. degrees in electrical engineering from the University of Stuttgart, Stuttgart, Germany, in 2016 and 2018, respectively, where he is currently pursuing the Ph.D. degree with the Institute of Smart Sensors.

He is also a Research Fellow in the Donhee Ham Lab at Harvard University, Cambridge, MA, USA. His current research interests include mixed-signal integrated circuits (ICs) for nuclear magnetic resonance (NMR), electron spin resonance (ESR), and biomedical applications.

Aoyang Zhang (Member, IEEE) received the B.S. degree from Zhejiang University, Hangzhou, China, in 2014, and the Ph.D. degree from the University of Southern California, Los Angeles, CA, USA, in 2020, all in electrical engineering.

He is currently a Post-Doctoral Fellow with Harvard University, Cambridge, MA, USA. His current research interests include threefold. First, analog/mixed-signal/radio frequency (RF)-integrated circuits (ICs) design for communications. Second, scalable nuclear magnetic resonance (NMR) and electron spin resonance (ESR)-based CMOS and GaN-integrated systems. Third, new circuit architecture with 2-D memristive devices.

Dr. Zhang was a recipient of the 2022 Harvard Teaching Award, the 2021 University of California (USC) Best Dissertation Award in Electrical Engineering, the 2020–2021 IEEE Solid-State Circuits Society (SSCS) Predoctoral Achievement Award, the 2020–2021 Ming Hsieh Institute Scholar, the IEEE SSCS Student Travel Grant Award (STGA) in 2018, the Best Bachelor Thesis Award in 2014, and the First Prize of Chinese National Mathematical Competition in 2010.

Behdad Aghelnejad was a Post-Doctoral Research Fellow with Harvard University, Cambridge, MA, USA, where he helped to develop low-field nuclear magnetic resonance (NMR) and magnetic resonance imaging (MRI) handheld devices. Before that, he has gained experience working on MRI, NMR, and Electron Paramagnetic Resonance (EPR)-related technologies at the École Normale Supérieure (ENS), Paris, France, and the Martin Luther University of Halle-Wittenberg, Halle, Germany. He is currently a part of the Oxford Instruments Magnetic Resonance Technology Team as a Senior Development Physicist.

Henry Hinton (Graduate Student Member, IEEE) received the B.S. degree in biomolecular engineering from the University of California, Santa Cruz, CA, USA, in 2018, and the M.S. and Ph.D. degrees in electrical engineering from Harvard University, Cambridge, MA, USA, in 2021 and 2023, respectively.

His current research interests include integrated circuit design for biological, optoelectronic, and electrochemical interfaces, and devices using emerging materials.

Victor Marrugat Arnal received the bachelor's degree in telecommunications technologies and services engineering and the bachelor's degree in engineering physics (double degree) from the Centre de Formació Interdisciplinària Superior (CFIS), Universitat Politècnica de Catalunya (UPC), Barcelona, Spain, in 2021. He is currently pursuing the M.S. degree in physics with ETH Zürich, Zürich, Switzerland. He finalized his bachelor's studies with a thesis at the Donhee Ham Research Group, Harvard University, Cambridge, MA, USA.

Yi-Qiao Song received the B.S. degree from Peking University, Beijing, China, in 1985, and the Ph.D. degree from Northwestern University, Xi'an, China, in 1991.

He was a Miller Research Fellow with the University of California at Berkeley, Berkeley, CA, USA, where he studied hyperpolarized gases. From 1997 to 2020, he worked with the Schlumberger-Doll Research, Cambridge, MA, USA, to develop nuclear magnetic resonance (NMR)/magnetic resonance imaging (MRI) for porous media and well logging. Currently, he is a Senior Scientist with Harvard University, Cambridge, and a Research Staff with the Massachusetts General Hospital, Boston, MA, USA. He has published over 160 articles in peer-reviewed scientific journals and holds over 60 patents.

Dr. Song is a fellow of the American Physical Society and the International Society of Magnetic Resonance, an Associate Editor of *Journal of Magnetic Resonance and Petroleum Sciences*, and a member of the Editorial Board of *Magnetic Resonance Letters* and *Chinese Journal of Magnetic Resonance*. He is also the Chair of the Magnetic Resonance in Porous Media Division, Groupement Ampere.

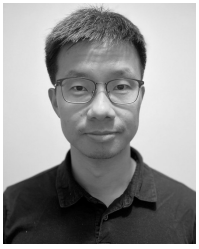

Yiqiao Tang received the Ph.D. degree from the Department of Physics, Harvard University, Cambridge, MA, USA, in 2013, where he discovered a fundamental quantity of light, optical chirality, and experimentally engineered its interaction with chiral materials in a nanophotonic structure.

Subsequently, he spent eight years at the Schlumberger-Doll Research, Cambridge, developing miniaturized nuclear magnetic resonance (NMR) sensors for subsurface exploration. Most recently, he joined Meta (then Facebook), Menlo Park, CA, USA, as a Data Scientist.

Ka-Meng Lei (Senior Member, IEEE) received the B.Sc. degree in electrical and electronic engineering (EEE) and the Ph.D. degree in electrical and computer engineering (ECE) from the University of Macau, Macau, in 2012 and 2016, respectively.

He was a Post-Doctoral Fellow with Harvard University, Cambridge, MA, USA, from 2017 to 2019, where he was involved in developing the high-resolution portable nuclear magnetic resonance (NMR) spectrometer. He has been serving as an Assistant Professor with the University of Macau since 2019. He has published 30 refereed articles. He coauthored one book *Handheld Total Chemical and Biological Analysis Systems: Bridging NMR, Digital Microfluidics, and Semiconductors* (Springer, 2018), and two book chapters *Micro-NMR on CMOS for Biomolecular Sensing* (Springer, 2018) and *Ultra-Low-Voltage Clock References* (Springer, 2023). His current research interests include ultralow voltage analog circuit techniques, sensors and analog front-end interfaces, and high-resolution portable NMR platforms.

Dr. Lei has been serving as a TPC Member for the IEEE International Conference on Integrated Circuits, Technologies and Applications (ICTA) since 2021. He is a Committee Member of the IEEE Solid-State Circuits Society (SSCS) Young Professionals, coordinating the Webinars for the Young Excellence Program. He was a (co-)recipient of the Best Paper Award at Asia Symposium on Quality Electronic Design (ASQED) in 2013, the Distinguished Design Award from the IEEE Asian Solid-State Circuits Conference (A-SSCC) in 2015, the Silkroad Award from International Solid-State Circuits Conference (ISSCC) in 2016, the Science and Technology Development Fund (FDCT) Macao Science and Technology Award for Postgraduates in 2016, the 2016 Young Researcher Award from the Instituto International de Macau, the IEEE SSCS Predoctoral Achievement Award in 2017, the Chipidea Microelectronics Prize in 2017 (Postgraduate), and the Best Poster Award from the Workshop on IC Advances in China (ICAC) in 2023. He was on the Organizing Committee of IEEE A-SSCC 2019. He is also an Associate Editor of the *IEEE Open Journal of Circuits and Systems*.

Jens Anders (Senior Member, IEEE) received the master's degree from the University of Michigan, Ann Arbor, MI, USA, in 2005, the Dipl.-Ing. degree from Leibniz University Hannover, Hannover, Germany, in 2007, and the Ph.D. degree from the École Polytechnique Fédérale de Lausanne (EPFL), Lausanne, Switzerland, in 2011.

From 2013 to 2017, he was an Assistant Professor of biomedical integrated sensors with the Institute of Microelectronics, University of Ulm, Ulm, Germany. Currently, he is a Full Professor and the Director of the Institute of Smart Sensors, University of Stuttgart, Stuttgart, Germany. Since 2022, he has been also the Co-Director of the Institute for Microelectronics Stuttgart (IMS CHIPS). He has authored or coauthored several books and book chapters and more than 150 journals and conference papers. His current research interests include circuit design for sensing applications, including materials science, and biomedical and quantum sensing.

Prof. Anders served as a Program Committee Member for European Solid-State Circuit Conference (ESSCIRC), ESSDERC, IEEE SENSORS JOURNAL, and International Solid-State Circuits Conference (ISSCC). He received the 2015 Information Technology Society (ITG) Publication Award, the Best Live Demo Award at the 2017 IEEE SENSORS JOURNAL, and the 2019 Helmholtz Center Berlin Technology Transfer Award, and one of the 2020 Sony Europe Research Awards. He was an Associate Editor of the IEEE TRANSACTIONS ON CIRCUITS AND SYSTEMS—II: EXPRESS BRIEFS and a Guest Editor of the IEEE JOURNAL OF SOLID-STATE CIRCUITS and IEEE SOLID-STATE CIRCUITS LETTERS.

Donhee Ham (Fellow, IEEE) is currently a Gordon McKay Professor of applied physics and electrical engineering with Harvard University, Cambridge, MA, USA, where he has been a Faculty Member since 2002, and is a Samsung Fellow. His current research is on: semiconductor-bio interfaces for neuroscience, machine intelligence, and biological data archiving; scalable nuclear magnetic resonance (NMR); integrated circuits; neuromorphic and in-sensor computing; and beyond CMOS electronics.